

# Topological nature of FeSe<sub>0.5</sub>Te<sub>0.5</sub> superconductor

Zhijun Wang<sup>\*\*</sup>,<sup>1,3</sup> P. Zhang<sup>\*\*</sup>,<sup>1</sup> Gang Xu,<sup>1,4</sup> L.K. Zeng,<sup>1</sup> H. Miao,<sup>1</sup> Xiaoyan Xu,<sup>1</sup> T. Qian,<sup>1</sup>  
Hongming Weng,<sup>1,2</sup> P. Richard,<sup>1</sup> A. V. Fedorov,<sup>5</sup> H. Ding,<sup>1,2,\*</sup> Xi Dai,<sup>1,2,†</sup> and Zhong Fang<sup>1,2,‡</sup>

<sup>1</sup>Beijing National Laboratory for Condensed Matter Physics,  
and Institute of Physics, Chinese Academy of Sciences, Beijing 100190, China

<sup>2</sup>Collaborative Innovation Center of Quantum Matter, Beijing, China

<sup>3</sup>Department of Physics, Princeton University, Princeton NJ 08544, USA

<sup>4</sup>Department of Physics, McCullough Building, Stanford University, Stanford CA 94305-4045, USA

<sup>5</sup>Advanced Light Source, Lawrence Berkeley National Laboratory, Berkeley, California 94720, USA

(Dated: September 12, 2018)

We demonstrate, using first-principles calculations, that the electronic structure of FeSe<sub>1-x</sub>Te<sub>x</sub> ( $x=0.5$ ) is topologically non-trivial, characterized by an odd  $\mathbb{Z}_2$  invariant and Dirac cone type surface states, in sharp contrast to the end member FeSe ( $x=0$ ). This topological state is induced by the enhanced three-dimensionality and spin-orbit coupling due to Te substitution (compared to FeSe), characterized by a band inversion at the  $Z$  point of the Brillouin zone, which is confirmed by our ARPES measurements. The results suggest that the surface of FeSe<sub>0.5</sub>Te<sub>0.5</sub> may support a non-trivial superconducting channel in proximity to the bulk.

PACS numbers: 73.43.-f, 74.70.Xa, 73.20.-r

Among the Fe-based superconductors, the FeSe<sub>1-x</sub>Te<sub>x</sub> family of compounds [1–4] is of particular interest. First, it has the simplest PbO structure (space group  $P4/nmm$ ) with Se (or Te) atoms forming distorted tetrahedra around Fe (see Fig. 1(a)) similar to the structure of FeAs planes in the families of FeAs-based high  $T_c$  superconductors [5]. Second, the internal parameters can be systematically tuned by the substitution of Se by Te [6–8], which provides us a platform for in-depth study of possible superconducting mechanisms and topological characters. Thirdly, superconductivity has been observed for a wide range of composition  $x$  [2–4], and the transition temperature  $T_c$  can be further enhanced by pressure [9–11]. More recently, superconductivity with  $T_c$  higher than 77 K was suggested for single unit cell FeSe films [12] epitaxially grown on SrTiO<sub>3</sub> substrates.

Despite these interesting properties though, the particularities of the system have still not been fully explored. Earlier studies, both theoretical and experimental, suggest the similarity of the electronic structures of the Fe chalcogenides (FeSe, FeTe) [13–15] and the FeAs-based [16–18] superconductors. Indeed, the low-energy physics around the Fermi level is dominated by the Fe- $3d$  states, and the morphology of the Fermi surfaces is similar. On the other hand, a surprisingly stable (no splitting under external magnetic field) zero-energy bound state (ZBS) at randomly distributed interstitial excess Fe sites was observed in very recent scanning tunneling microscopy (STM) measurements on the surface of superconducting Fe(Te,Se) [19], suggesting possible topological feature of its electronic structure. Obviously, the

$5p$  orbitals of Te are more extended and have stronger spin-orbit coupling (SOC) than the  $4p$  orbitals of Se. The consequences of Te substitution, particularly for the bulk topological character of FeSe<sub>1-x</sub>Te<sub>x</sub>, have been largely ignored in the literature and will be the main purpose of the present paper. Based on first-principles calculations combined with angle resolved photoemission spectroscopy (ARPES) measurements, here we report that the electronic structure of FeSe<sub>0.5</sub>Te<sub>0.5</sub> is topologically non-trivial, in sharp contrast to its end member FeSe. The topological properties of FeSe<sub>0.5</sub>Te<sub>0.5</sub> can be characterized by an odd  $\mathbb{Z}_2$  number, and the existence of Dirac cone type surface states, in proximity to bulk superconductivity, should favor topologically superconducting surface states, as suggested by Fu and Kane [20].

The electronic structures of FeSe and FeSe<sub>0.5</sub>Te<sub>0.5</sub> are calculated with SOC included. The calculations are performed based on the density functional theory (DFT) [21, 22] and the generalized gradient approximation (GGA) for the exchange-correlation potential [23], as implemented in the plane-wave pseudopotential based BSTATE (Beijing Simulation Tool of Atomic TEchnology) package [24]. The experimental lattice parameters [6] are used in the calculations. Maximally localized Wannier functions (MLWF) [25] are constructed from bulk calculations, and then used to study the surface states in the semi-infinite system. To treat the substitution properly, we have calculated FeSe<sub>0.5</sub>Te<sub>0.5</sub> by using both the virtual crystal approximation and the two-formula cell with ordered Se and Te sites. Both calculations give converging results.

We first neglect the SOC and concentrate on the comparison between the electronic structures of FeSe and FeSe<sub>0.5</sub>Te<sub>0.5</sub> (as shown in Fig. 1 (c) and (d)). The band structure of FeSe is very similar to that of LaOFeAs as

<sup>\*\*</sup>these authors contributed equally to this work.

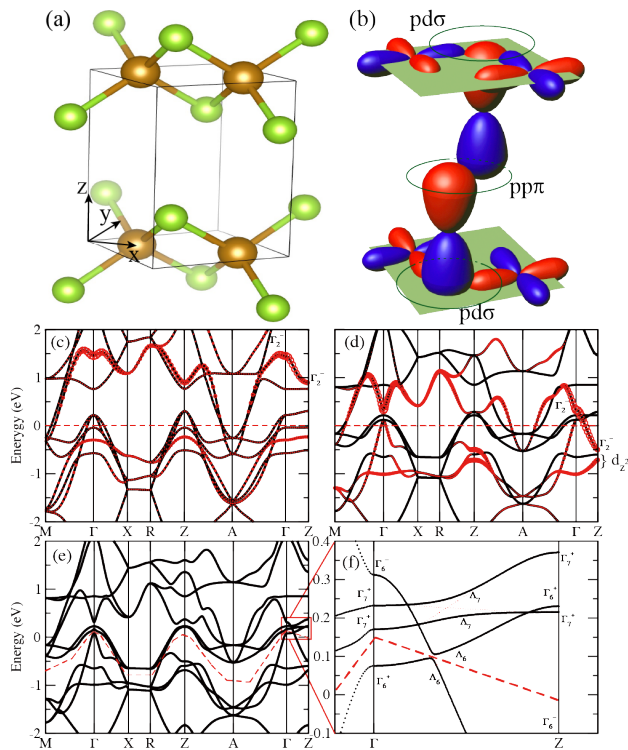


FIG. 1: (Color online) The crystal structure and DFT electronic band structures of FeX ( $X = \text{Se}_{0.5}\text{Te}_{0.5}$ ). (a) is the crystal structure with the  $x$ -axis pointing along Fe nearest neighbors. Grey and green balls represent Fe and X atoms, respectively. (b) Schematic plot of the hybridization along the  $z$  axis between the combined orbitals  $D_{xy}^-$  and  $P_z^-$  (see details in appendix B), consisting of intralayer  $pd\sigma$  and interlayer  $pp\pi$  hopping. (c) Band structure of FeSe with internal parameter  $z_X=0.2345$  without SOC. (d) Band structure of  $\text{FeSe}_{0.5}\text{Te}_{0.5}$  ( $z_X=0.2719$ ) without SOC. (e) Band structure of  $\text{FeSe}_{0.5}\text{Te}_{0.5}$  with SOC. (f) Zoom-in view of the solid red box area in (e). The size of red the circles in (c) and (d) indicates the weight of the  $p_z$  component of the chalcogen atoms. The two  $d_{z^2}$  bands are indicated below  $E_F$  in (d). The original  $\Lambda_5$  bands split into  $\Lambda_6$  and  $\Lambda_7$ . Along the  $\Gamma$ - $Z$  line, two  $\Lambda_6$  bands cross and hybridize to open a SOC gap of about 10 meV. The red dashed line corresponds to a Fermi curve across the gap.

reported before [17]. At the  $\Gamma$  point, the valence band top is not occupied, leading to the well known hole pockets of Fermi surfaces around  $\Gamma$ . The three top-most states at  $\Gamma$  can be labeled as two-fold degenerate  $\Gamma_5^+$  states ( $d_{yz}/d_{xz}$  orbitals) and non degenerate  $\Gamma_4^+$  state ( $d_{xy}$  orbital), respectively. There is a clear band gap larger than 0.6 eV above the valence band top at the  $\Gamma$  point. All the  $d-d$  anti-bonding states (with negative parity) are located above the gap except the  $d_{z^2}$  orbital that has a weaker anti-bonding state. Among them, the most interesting state is the second highest one with remarkable red circles, which belongs to the  $\Gamma_2^-$  representation and comes from the anti-bonding  $d_{xy}$  orbitals of Fe and  $p_z$  orbital of chalcogen. The weight of the  $p_z$  component is

illustrated by the size of red circles, which suggests that the  $\Gamma_2^-$  state can be affected by hybridizing with the  $d_{xy}$  and  $p_z$  orbitals. Looking along the  $\Gamma-Z$  direction, the band dispersion of the  $\Gamma_2^-$  state is the strongest among all  $d$  states. Nevertheless, since it is energetically high, the band structure around the  $Z$  point of the Brillouin zone (BZ) is only slightly affected and remains similar to that around  $\Gamma$ . The result suggests that FeSe is quite two-dimensional with strong anisotropy.

Immediate differences can be seen in comparing these results with the band structure of  $\text{FeSe}_{0.5}\text{Te}_{0.5}$  shown in Fig. 1(d): (1) the  $\Gamma_2^-$  state in  $\text{FeSe}_{0.5}\text{Te}_{0.5}$  is significantly pushed down and almost touches the valence band top, and the band gap at  $\Gamma$  (above the valence and top) is nearly closed; (2) the band dispersion of this  $\Gamma_2^-$  state along the  $\Gamma-Z$  direction is strongly enhanced. As a result, a band inversion occurs at the  $Z$  point, which implies a change of topological property.

Compared to FeSe, the  $c$ -axis and the experimental intra-layer distance  $d_z$  of  $\text{FeSe}_{0.5}\text{Te}_{0.5}$  are enlarged by 8.2% and 11%, respectively (See appendix A), while the  $a$ -axis and the inter-layer distance change only very little. As a result, the intra-layer hybridizations, especially the  $pd\sigma$  hopping as shown in Fig. 1(b), are seriously weakened, and the  $\Gamma_2^-$  band center is lowered very much and becomes close to  $E_F$ , as shown in Fig. 1(d). On the other hand, because the Te 5 $p$  orbitals are much more extended than the Se 4 $p$  orbitals, the inter-layer hybridization through the  $pp\pi$  bonding becomes stronger. Therefore, the Te substitution enhances the hopping between layers and gives rise to a larger dispersion for  $\Gamma_2^-$  in  $\text{FeSe}_{0.5}\text{Te}_{0.5}$ . These two observations are in good agreement with the band structure of  $\text{FeSe}_{0.5}\text{Te}_{0.5}$  shown in Fig. 1(d). Therefore, the band inversion in  $\text{FeSe}_{0.5}\text{Te}_{0.5}$  is a consequence of the weakened intra-layer hopping and enhanced inter-layer hopping originating from the Te substitution.

Once SOC is included, the band structure of  $\text{FeSe}_{0.5}\text{Te}_{0.5}$  opens a direct SOC gap and a non-trivial  $\mathbb{Z}_2$  invariant can be defined by assuming a “curved chemical potential”—the red dashed line in Fig. 1(e)—lying between the 10th and 11th bands (neglecting the spin-doublet degeneracy of the bands). Generally, the doubly degenerate  $\Gamma_5^+$  states split into  $\Gamma_6^+$  and  $\Gamma_7^+$ , and the odd  $\Gamma_2^-$  state turns into  $\Gamma_6^-$  (see details in appendix B). Along the  $\Gamma$ - $Z$  high-symmetry line, two  $\Lambda_6$  bands under  $C_{4v}$  symmetry hybridize and open a gap of about 10 meV, which is clearly shown in Fig. 1(f). When defining a Fermi curve through the SOC gap, the  $\mathbb{Z}_2$  invariant is easily calculated from the parity criterion, which comes out to 1. (The parities at all time-reversal invariant momenta (TRIM) are presented in appendix B.) This non-zero  $\mathbb{Z}_2$  invariant indicates that  $\text{FeSe}_{0.5}\text{Te}_{0.5}$  is in a topological phase that can support the non-trivial surface states (SS). Due to the substantial SOC of Te, increasing the content  $x$  enlarges the SOC gap, which is benefi-

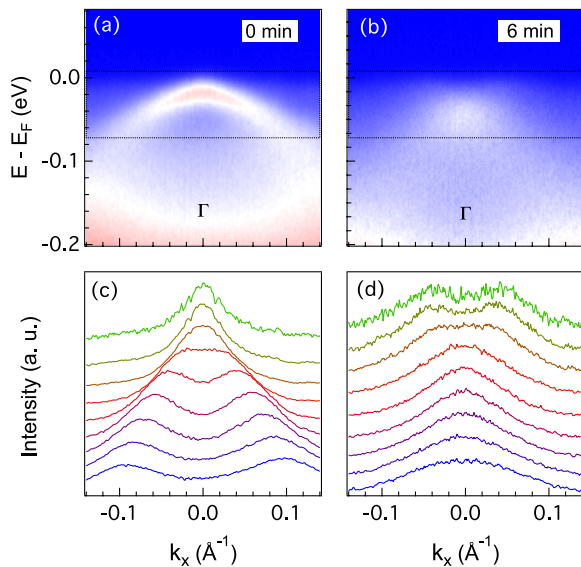


FIG. 2: (Color online) ARPES spectra along the  $\Gamma$ -M direction in the  $\sigma$  polarization geometry. (a)  $\text{FeSe}_{0.5}\text{Te}_{0.5}$  before surface evaporation. (b)  $\text{FeSe}_{0.5}\text{Te}_{0.5}$  after 6 minutes of K surface doping. (c), (d) MDCs corresponding to data from the dash boxes in panels (a) and (b), respectively.

cial for the detection of the SS in the gap. Moreover, we also performed dynamical mean-field theory (DMFT) calculations to confirm the band inversion and identify the strong band renormalization due to electronic correlations (see appendix C for details). The correlation effects do not change the detail of the electronic bands, but simply reduce the bandwidth.

We performed ARPES measurements in order to demonstrate experimentally the existence of the  $\Gamma_2^-$  band with strong  $p_z$  orbital character crossing  $E_F$  along the  $\Gamma$ -Z direction. Large single-crystals of  $\text{FeSe}_{0.45}\text{Te}_{0.55}$  were grown using the self-flux method, and  $\text{LiFeAs}$  with FeAs flux method. ARPES measurements were performed at the Advanced Light Source and Synchrotron Radiation Center, using a VG-Scienta electron analyzer. The light used was linearly polarized in directions parallel to the analyzer slit. The K source used for evaporation is made of a SAES K dispenser. In the experiments, the largest coverage is less than one mono-layer. All data were recorded with linear horizontal polarized photons with a vertical analyzer slit ( $\sigma$  geometry). Under this configuration, odd orbitals with respect to the emission plane are visible, such as the  $d_{xy}$  and  $d_{yz}$  orbitals, while the  $d_{xz}$  band should not be detected. In addition, our experimental setup leads to a  $z$  component of the light polarization, and thus orbitals with mainly  $z$  components such as  $d_{z^2}$  and  $p_z$  orbitals are also observable [26].

The comparison of the DFT band calculations on FeSe and  $\text{FeSe}_{0.5}\text{Te}_{0.5}$ , shown in Figs. 1(c) and 1(d), suggests that while it is pushed far above  $E_F$  at  $\Gamma$  in FeSe, the  $\Gamma_2^-$  band in  $\text{FeSe}_{0.5}\text{Te}_{0.5}$  forms an electron band just above

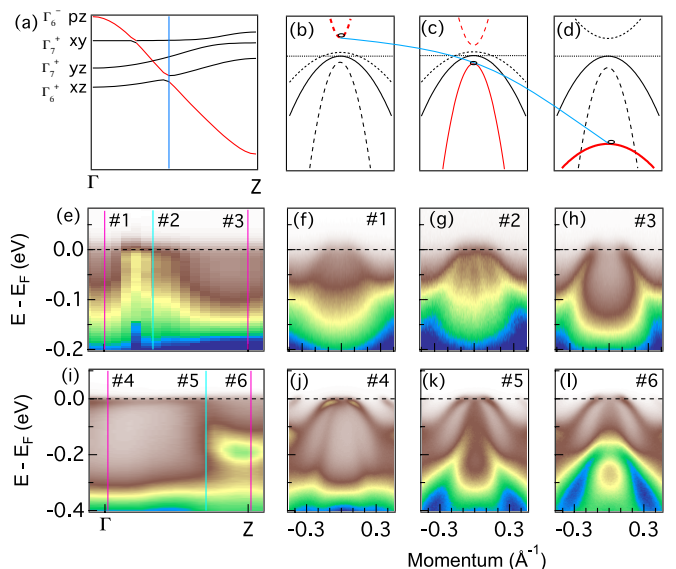


FIG. 3: (Color online) Normal emission ARPES spectra. First row: schematic band dispersions. Second row: ARPES data on  $\text{FeSe}_{0.5}\text{Te}_{0.5}$ . Third row: ARPES data on  $\text{LiFeAs}$ . First column: dispersion at  $k_x = 0$  along the  $\Gamma$ -Z direction. Second, third and fourth columns: electronic dispersions along cuts indicated in the first column.

$E_F$ . To prove its existence, we raised the chemical potential by performing *in-situ* K doping, and we measured ARPES spectra along  $\Gamma$ -M at  $h\nu = 30$  eV, which coincides with  $k_z = 0$  [27]. The results before and after evaporation (6 minutes) are shown in Figs. 2(a) and 2(b), respectively. As expected, the hole band is sinking further below  $E_F$  after evaporation. Interestingly, an additional electron band is observed, as clearly shown by contrasting the momentum distribution curves (MDCs) obtained before (Fig. 2(c)) and after (Fig. 2(d)) evaporation. This band, locating about 30 meV above the top of the valence band in  $\text{FeSe}_{0.5}\text{Te}_{0.5}$ , is very similar to the small 3D electron pocket reported in  $(\text{Tl,Rb})_y\text{Fe}_{2-x}\text{Se}_2$  [26], which mainly has a  $p_z$  component.

In the presence of SOC, the DFT calculations indicate that the  $\Gamma_6^-$ ,  $\Gamma_7^+$  and  $\Gamma_7^+$  states at the  $\Gamma$  point mostly come from the  $d_{xz}$ ,  $d_{yz}$  and  $d_{xy}$  orbitals, respectively, while the  $\Gamma_6^-$  state (labeled as  $\Gamma_2^-$  without SOC) have an important  $p_z$  component besides the  $d_{xy}$  orbital. As shown in Fig. 3(a), while the  $p_z$  band locates above  $E_F$  at  $\Gamma$ , it is shifted below  $E_F$  upon moving along  $\Gamma$ -Z and it reaches its minimum at the Z point. On its way down, the  $p_z$  band crosses the  $d_{xy}$ ,  $d_{yz}$  and  $d_{xz}$  bands, opening a SOC gap with the  $d_{xz}$  band. This situation is illustrated schematically in Fig. 3(a). We now ask how the hybridization of the  $p_z$  band with the  $d_{xz}$  band should affect the ARPES measurements. Around the  $\Gamma$  point, the  $p_z$  band forms an electron-like band located above  $E_F$  along the  $\Gamma$ -M direction. Therefore, it should not be observed in our experimental geometry. Due to selec-

tion rules, the  $d_{xz}$  band should not be observed either and only the  $d_{xy}$  and  $d_{yz}$  band can possibly be seen, as shown schematically in Fig. 3(b). However, because it hybridizes with the  $p_z$  band, one should expect to be able to detect the  $d_{xz}$  band near the crossing point below  $E_F$ , as illustrated schematically in Fig. 3(c). Finally, our calculations indicate that the  $p_z$  band has a hole-like dispersion near the Z point, and we should be able to observe it. On the other hand, the  $d_{xz}$  band no longer hybridizes strongly with the  $p_z$  band and its intensity should be significantly suppressed again in the  $\sigma$  polarization, as described in Fig. 3(d).

In order to confirm this dispersion, we compare in Fig. 3(e) ARPES spectra recorded on  $\text{FeSe}_{0.45}\text{Te}_{0.55}$  with different photon energies. We see some intensity between the  $\Gamma$  and Z points that we assign to the  $p_z$  band sinking down from  $\Gamma$  to Z. At the Z point, this band has merged with the strong  $d_{z^2}$  band and it is thus undistinguishable. We display in Figs. 3(f)-3(h) three ARPES intensity cuts along  $\Gamma$ -M recorded on  $\text{FeTe}_{0.55}\text{Se}_{0.45}$  and corresponding respectively to  $k_z$  values around  $\Gamma$  (Cut#1, Fig. 3(f)), the hybridization between the  $p_z$  and  $d_{xz}$  bands (Cut#2, Fig. 3(g)), and around Z (Cut#3, Fig. 3(h)). As the  $d_{xy}$  band heavily renormalizes compared to the  $d_{xz}/d_{yz}$  bands, it is shallower and hardly resolved with weaker intensity [28]. In Cut#1 (Fig. 3(f)), as expected, none of the  $p_z$  and  $d_{xz}$  bands are detected near  $k_z = 0$ . In contrast, not only the  $d_{yz}$  band is observed in Cut#2 (Fig. 3(g)), but the  $d_{xz}$  band as well due to its hybridization with the  $p_z$  band. At the Z point, away from hybridization, the  $d_{xz}$  band disappears from the ARPES spectrum (Fig. 3(h)). Unfortunately, the  $p_z$  band is too close to the strong  $d_{z^2}$  band to be distinguished unambiguously.

As shown in Figs. 3(i) to 3(l), the strong  $k_z$  dispersion of the  $p_z$  band is also observed in  $\text{LiFeAs}$ , which exhibits very clear spectral features. Because its bottom is located away from the  $d_{z^2}$  band, the dispersion of the  $p_z$  band along  $\Gamma$ -Z can be identified very clearly, as illustrated in Fig. 3(i). As with  $\text{FeSe}_{0.45}\text{Te}_{0.55}$ , the intensity of the  $d_{xz}$  band is the strongest along Cut#5 (Fig. 3(k)), where it hybridizes with the  $p_z$  band. Figs. 3(k)-3(l) also show clearly that the  $p_z$  band has a hole-like dispersion below  $E_F$ , as expected theoretically.

Finally, we analyze the spin-resolved Fermi surfaces around the Dirac point of the semi-infinite system formed by the SS to identify the non-trivial topology. With the surface Green's function calculated from the modified effective Hamiltonian considering DMFT on-site modification, the spin-filter surface states and the corresponding Fermi surfaces can be obtained directly. From the dispersion of the SS shown in Fig. 4(a), the protected SS emerges in the SOC gap around  $E_F$  due to the non-trivial topological nature of the bulk system. The Fermi surface of the SS ( $E_F = 50$  meV) is illustrated as a bright yellow circle in Fig. 4(b), and the spin orientation for the

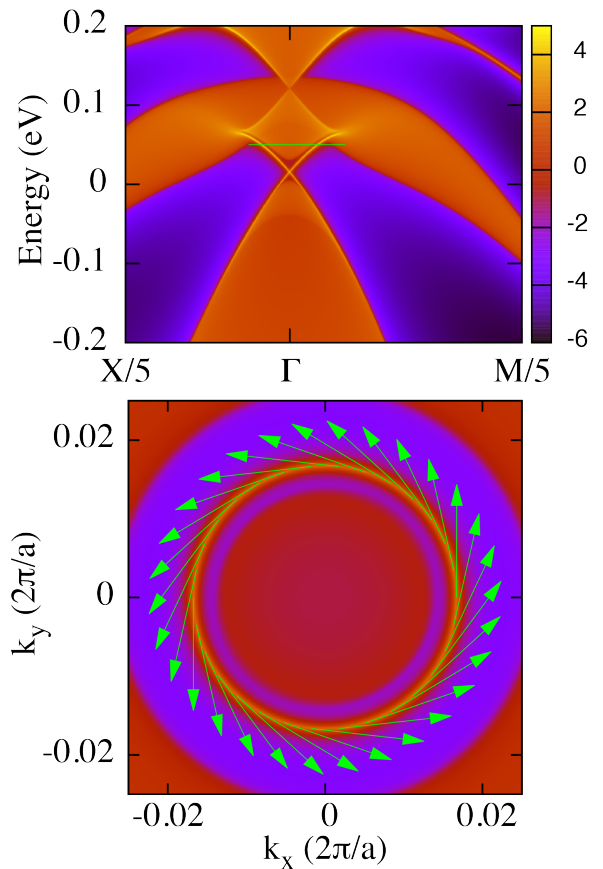


FIG. 4: (Color online) Topological non-trivial 001 surface states and spin-resolved Fermi surface of these states. (a) Surface LDOS on the (001) surface for  $\text{FeSe}_{0.5}\text{Te}_{0.5}$  considering DMFT on-site modification. (b) Fermi surface of the topological state (bright yellow circle beside the projected bulk states). The in-plane spin orientation is indicated by green arrows.

SS around the Fermi surface is marked by green arrows, which form a  $\pi$  Berry phase enclosed. The magnitude of the  $z$  spin component is very small compared to the in-plane component. The  $\pi$  Berry phase signifies the topological non-trivial properties of the bulk. By inducing a  $s$ -wave superconducting gap, the chiral SS can play an important role to produce the Majorana zero mode.

In conclusion, we have presented both theoretical and experimental evidences for a topological non-trivial phase in  $\text{FeSe}_{0.5}\text{Te}_{0.5}$ . From the DFT calculations, we show that the band topology is sensitive to the intra-layer and inter-layer hopping terms, which can be tuned by the Te substitution. The Te substitution content  $x$  strongly affects the structural, electronic and topological properties of these materials. We have identified the topologically non-trivial electronic band structure of  $\text{FeSe}_{0.5}\text{Te}_{0.5}$  with a band inversion, characterized by an odd  $\mathbb{Z}_2$  invariant and spin-moment locked SS. Our ARPES data strongly support that the  $\Gamma_2^-$  band forms a band inversion at the

Z point. The similar results can also be applied to ironpnictides such as LiFeAs. Due to the topological non-trivial surface states, the  $\text{FeSe}_{1-x}\text{Te}_x$  materials would be an ideal system for realizing possible topological superconductor and Majorana fermions on the surface.

We acknowledge discussions with J.P. Hu and experimental assistance from Y.M. Xu. This work was supported by NSFC (11474340, 11274362, 11204359 and 11234014), the 973 program of China (2011CBA001000, 2011CBA00108 and 2013CB921700), and the ‘‘Strategic Priority Research Program (B)’’ of the Chinese Academy of Sciences (XDB07000000 and XDB07020100).

---

\* Electronic address: dingh@aphy.iphy.ac.cn

† Electronic address: daix@aphy.iphy.ac.cn

‡ Electronic address: zfang@aphy.iphy.ac.cn

- [1] F.-C. Hsu, J.-Y. Luo, L.-W. Yeh, T.-K. Chen, T.-W. Huang, P. M. Wu, Y.-C. Lee, Y.-L. Huang, Y.-Y. Chu, D.-C. Yan, and M.-K. Wu, Proc. Natl. Acad. Sci. U.S.A. **105**, 14262 (2008).
- [2] K.-W. Yeh, T.-W. Huang, Y.-L. Huang, T.-K. Chen, F.-C. Hsu, P. M. Wu, Y.-C. Lee, Y.-Y. Chu, C.-L. Chen, J.-Y. Luo, D.-C. Yan, and M.-K. Wu, Europhys. Lett. **84**, 37002 (2008).
- [3] M. H. Fang, H. M. Pham, B. Qian, T. J. Liu, E. K. Vehstedt, Y. Liu, L. Spinu, and Z. Q. Mao, Phys. Rev. B **78**, 224503 (2008).
- [4] B. C. Sales, A. S. Sefat, M. A. McGuire, R. Y. Jin, D. Mandrus, and Y. Mozharivskyj, Phys. Rev. B **79**, 094521 (2009).
- [5] Y. Kamihara, T. Watanabe, M. Hirano, and H. Hosono, J. Am. Chem. Soc. **130**, 3296 (2008).
- [6] Shiliang Li, Clarina de la Cruz, Q. Huang, Y. Chen, J. W. Lynn, Jiangping Hu, Yi-Lin Huang, Fong-Chi Hsu, Kuo-Wei Yeh, Maw-Kuen Wu, and Pengcheng Dai, Phys. Rev. B **79**, 054503 (2009).
- [7] X. Wu *et al.*, arXiv:1412.3375 (2014)
- [8] L. C. C. Ambolode II *et al.*, arXiv:1505.07637 (2015)
- [9] Y. Mizuguchi, F. Tomioka, S. Tsuda, T. Yamaguchi, and Y. Takano, Appl. Phys. Lett. **93**, 152505 (2008).
- [10] S. Medvedev, T. M. McQueen, I. A. Troyan, T. Palasyuk, M. I. Eremets, R. J. Cava, S. Naghavi, F. Casper, V. Ksenofontov, G. Wortmann, and C. Felser, Nature Mater. **8**, 630 (2009).
- [11] S. Margadonna, Y. Takabayashi, Y. Ohishi, Y. Mizuguchi, Y. Takano, T. Kagayama, T. Nakagawa, M. Takata, and K. Prassides, Phys. Rev. B **80**, 064506 (2009).
- [12] J. J. Lee *et al.* Nature **515**, 245-248 (2014).
- [13] A. Subedi, L. Zhang, D. J. Singh, and M. H. Du, Phys. Rev. B **78**, 134514 (2008).
- [14] M. Aichhorn, S. Biermann, T. Miyake, A. Georges, and M. Imada, Phys. Rev. B **82**, 064504 (2010).
- [15] A. Tamai *et al.* Phys. Rev. Lett. **104**, 097002 (2010).
- [16] I. A. Nekrasov *et al.*, JETP Lett. **87**, 560 (2008).
- [17] G. Xu, W. Ming, Y. Yao, X. Dai, S.-C. Zhang and Z. Fang, Europhys. Lett. **82**, 67002 (2008).
- [18] K. Haule, J. H. Shim, and G. Kotliar, Phys. Rev. Lett. **100**, 226402 (2008).
- [19] J.-X. Yin, Zheng Wu, J.-H. Wang, Z.-Y. Ye, Jing Gong, X.-Y. Hou, Lei Shan, Ang Li, X. -J. Liang, X.-X. Wu, Jian Li, C.-S. Ting, Z. Wang, J.-P. Hu, P.-H. Hor, H. Ding, and S. H. Pan, arXiv:1403.1027 (unpublished).
- [20] L. Fu and C. L. Kane, Phys. Rev. Lett. **100**, 096407 (2008).
- [21] P. Hohenberg and W. Kohn, Phys. Rev. **136**, B864 (1964).
- [22] W. Kohn and L. J. Sham, Phys. Rev. **140**, A1133 (1965).
- [23] J. P. Perdew, K. Burke, and M. Ernzerhof, Phys. Rev. Lett. **77**, 3865 (1996).
- [24] Z. Fang and K. Terakura, J. Phys.: Condens. Matter **14**, 3001 (2002).
- [25] I. Souza, N. Marzari and D. Vanderbilt, Phys. Rev. B **65**, 035109 (2001).
- [26] Z.-H. Liu *et al.*, Phys. Rev. Lett. **109**, 037003 (2012)
- [27] P. Zhang *et al.*, Appl. Phys. Lett. **105**, 172601 (2014)
- [28] M. Yi *et al.*, Phys. Rev. Lett. **110**, 067003 (2013).
- [29] R. Juza and K. Langer, Z. Anorg. Allg. Chem. **361**, 58 (1982).
- [30] Z. Wang and S.-C. Zhang, Phys. Rev. X **2**, 031008 (2012).
- [31] Z. Wang, X.-L. Qi, and S.-C. Zhang, Phys. Rev. B **85**, 165126 (2012).

## Appendix A: Structural parameters of FeX and band structure of LiFeAs

TABLE I: Structural parameters of PbO-structure FeX. The lattice parameters are from experimental data [6], and both optimized (Opt.) and experimental (Exp.) internal chalcogen positions  $z_X$  are shown.  $d_z$  is the cartesian distance in the  $z$  direction from the X plane to the Fe plane.

	a (Å)	c (Å)	$z_X$ (Opt.)/ $d_z$ (Å)	$z_X$ (Exp.)/ $d_z$ (Å)
FeSe	3.784	5.502	0.2345/1.2902	0.2652/1.4591
FeTe	3.8215	6.2695	0.2496/1.5648	0.2829/1.7736
FeSe <sub>0.5</sub> Te <sub>0.5</sub>	3.7933	5.9552	0.2476/1.4745	0.2719/1.6192

For LiFeAs, we used the experimental lattice parameters [29] and relaxed the free internal coordinates. The experimental structure (space group P4/nmm, 129) has the Li sites in 2c positions, which lie above and below the centers of the Fe squares opposite the As. The calculated DFT band structure is given in Fig. 5. The  $\Gamma_2^-$  band shows a large dispersion and a band reversion along the  $z$  direction.

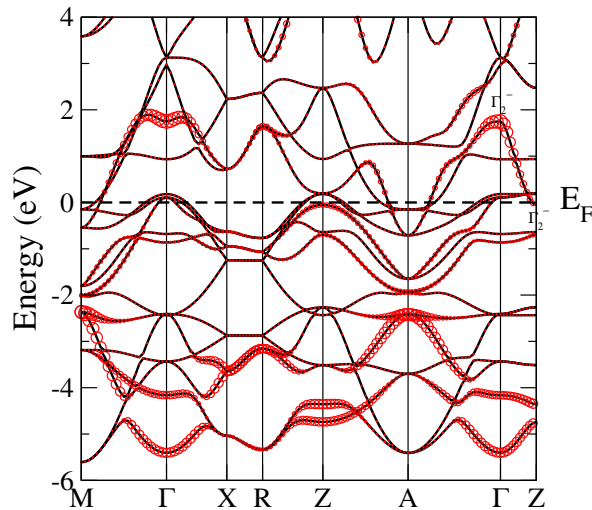


FIG. 5: (Color online) Electronic band structure of LiFeAs. The  $p_z$  component is highlighted by the size of the red circles.

## Appendix B: Symmetry and parity analysis

Since the system has inversion symmetry, it is convenient to combine these orbitals into bonding and antibonding states with definite parity as

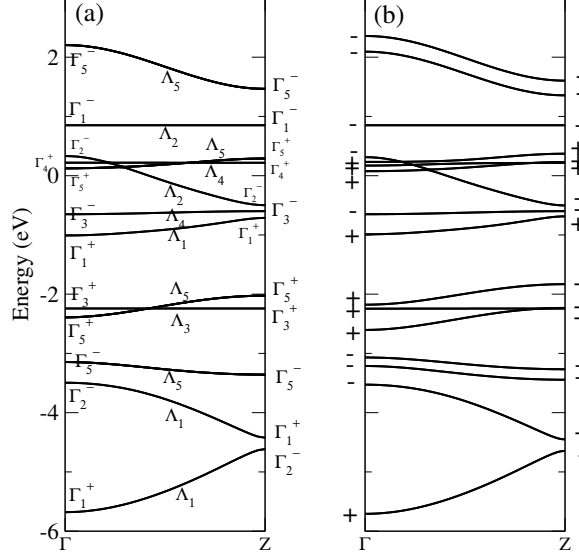
$$|D_\alpha^\pm\rangle = \frac{1}{\sqrt{2}}(|Fe_\alpha\rangle \pm |Fe'_\alpha\rangle),$$

$$|P_\beta^\pm\rangle = \frac{1}{\sqrt{2}}(|X_\beta\rangle \mp |X'_\beta\rangle)$$

Using the orbitals with definite parity defined in the main text, we can label all the non-spin-orbital (NSO) bands with the irreducible representations (IRs), which are given in Table II. The  $\Gamma_2^-$  band is composed of the antibonding states with both  $d_{xy}$  and  $p_z$  characters. At both the  $\Gamma$  and Z points, the IRs of the  $D_{4h}$  group are labeled as  $\Gamma_n^\pm$ , whereas along the  $\Gamma$ -Z high-symmetry line, we label these IRs as  $\Lambda_n$  because of its  $C_{4v}$  symmetry. In our conventions, the  $(x,y)$  axes are rotated by  $45^\circ$  as compared to the crystallographic axes, so that the  $d_{xy}$  orbital in our definition is the one pointing from Fe to chalcogen atoms, as shown in Fig. 1.

TABLE II: Combined orbitals and related irreducible representations

D/P (+/-)	$z^2$	$yz/xz$	$xy$	$x^2-y^2$	$x/y$	$z$
$D_{4h}$	+	$\Gamma_1^+$	$\Gamma_5^+$	$\Gamma_4^+$	$\Gamma_3^+$	$\Gamma_5^+$ $\Gamma_1^+$
	-	$\Gamma_3^-$	$\Gamma_5^-$	$\Gamma_2^-$	$\Gamma_1^-$	$\Gamma_5^-$ $\Gamma_2^-$
$C_{4v}$	+	$\Lambda_1$	$\Lambda_5$	$\Lambda_4$	$\Lambda_3$	$\Lambda_5$ $\Lambda_1$
	-	$\Lambda_4$	$\Lambda_5$	$\Lambda_1$	$\Lambda_2$	$\Lambda_5$ $\Lambda_1$

FIG. 6: (Color online) Electronic band structure along  $\Gamma$ -Z. (a) The IRs are labeled in the NSO bands. (b) The parities are labeled in the SOC bands.

The IR labels along the  $\Gamma$ -Z line are shown in Fig. 6(a). Around  $E_F$ , the  $D_{xz/yz}^+$  bands can mix with the  $P_{x/y}^+$  orbitals with the same  $\Gamma_5^+$  representations, although the P-D hybridization is not strong due to the little orbital overlap in the real space. For the  $\Gamma_2^-$  representation, the  $D_{xy}^-$  character can mix with the  $P_z^-$  band, and the  $d_{xy}$  and  $p_z$  orbitals have a strong hybridization along the  $z$  direction. However,  $d_z$  becomes larger with the Te substitution content  $x$  increasing, thus leading to weaker hybridization. As a result, the  $\Gamma_2^-$  band, consisting of  $d_{xy}$  and  $p_z$  orbitals, sinks down to  $E_F$  and has a large dispersion in FeSe<sub>0.5</sub>Te<sub>0.5</sub>. Moreover, due to selection rules, the bonding state of  $D_{xy}^+$  cannot mix with the  $p_z$  band, including along the  $\Gamma$ -Z line. As a consequence, the  $\Gamma_4^+$  band characterized by the  $D_{xy}^+$  representation exhibits a weak dispersion in the  $z$  direction, which is not sensitive to the height  $d_z$ . Beside, all the IRs in NSO bands and parities in SOC bands are presented in Table III. “(+, -)” denotes that the quadruple bands consist of two Kramers pairs with opposite parity. The non-trivial  $\mathbb{Z}_2$  index is presented beside the vertical line, which denotes the hypothetical Fermi level in the main text.

### Appendix C: LDA+DMFT confirmation

The LDA + DMFT method has proven to be a powerful technique to study the electronic structure of correlated systems. In this section, we apply this method to FeSe<sub>0.5</sub>Te<sub>0.5</sub> with a local Coulomb integral  $U=F_0=4.0$  eV and a Hund’s coupling  $J=0.7$  eV, and confirm that it has a topological character of band inversion by computing the topological invariants within the DMFT framework.

The one-electron spectral function is defined as

$$A_{\mathbf{k}}(\omega) = -\frac{1}{\pi} \frac{Im\Sigma(\omega)}{(\omega + \mu - \epsilon_{\mathbf{k}} - Re\Sigma(\omega))^2 + Im\Sigma(\omega)^2}$$

TABLE III: The  $D_{4h}$  IRs and parities for each band.

IRs(NSO)	P										D						
	$\Gamma_1^+$	$\Gamma_2^-$	$\Gamma_5^-$	$\Gamma_5^+$	$\Gamma_3^+$	$\Gamma_1^+$	$\Gamma_3^-$	$\Gamma_5^+$	$\Gamma_4^+$	$\Gamma_2^-$	$\Gamma_1^-$	$\Gamma_5^-$	$\Gamma_4^+$	$\Gamma_5^+$	$\Gamma_2^-$	$\Gamma_1^-$	$\Gamma_5^-$
Z	$\Gamma_2^-$	$\Gamma_1^+$	$\Gamma_5^-$	$\Gamma_3^+$	$\Gamma_5^+$	$\Gamma_3^+$	$\Gamma_1^+$	$\Gamma_3^-$	$\Gamma_2^-$	$\Gamma_4^+$	$\Gamma_5^+$	$\Gamma_2^-$	$\Gamma_4^+$	$\Gamma_5^+$	$\Gamma_1^-$	$\Gamma_5^-$	
Parities(SO)	1	2	3	4	5	6	7	8	9	10	11	12	13	14	15	16	
$\Gamma$	+	-	-	-	+	+	+	+	-	+	+	+	-	-	-	-	
Z	-	+	-	-	+	+	+	+	-	-	+	+	+	-	-	-	
X	(+ -)	(+ -)	(+ -)	(+ -)	(+ -)	(+ -)	(+ -)	(+ -)	(+ -)	(+ -)	(+ -)	(+ -)	(+ -)	(+ -)	(+ -)	(+ -)	
M	(+ -)	(+ -)	(+ -)	(+ -)	(+ -)	(+ -)	(+ -)	(+ -)	(+ -)	(+ -)	(+ -)	(+ -)	(+ -)	(+ -)	(+ -)	(+ -)	
R	(+ -)	(+ -)	(+ -)	(+ -)	(+ -)	(+ -)	(+ -)	(+ -)	(+ -)	(+ -)	(+ -)	(+ -)	(+ -)	(+ -)	(+ -)	(+ -)	
A	(+ -)	(+ -)	(+ -)	(+ -)	(+ -)	(+ -)	(+ -)	(+ -)	(+ -)	(+ -)	(+ -)	(+ -)	(+ -)	(+ -)	(+ -)	(+ -)	
$Z_2$										1							

in terms of the LDA band dispersion  $\epsilon_{\mathbf{k}}$  and the self-energy  $\Sigma(\omega)$ . This momentum-resolved spectra  $A_{\mathbf{k}}(\omega)$  is shown in the upper panel of Fig. 7, where the overall renormalization of the bands and the bandwidth reduction are apparent. However, the relative positions of different bands almost do not change. The  $\Gamma_2^-$  and  $\Gamma_5^+$  bands crossing near  $E_F$  remains in the correlated system.

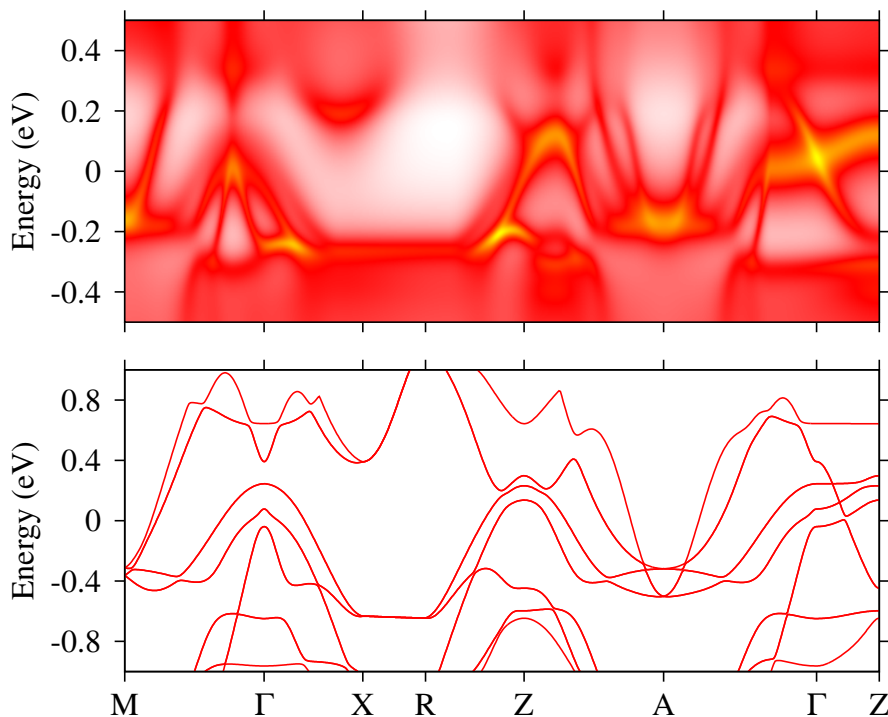


FIG. 7: (Color online) (Upper panel) LDA+DMFT calculations. (Lower panel) SOC band structure only taking the LDA+DMFT on-site modification into consideration.

In a previous work [30], only the Green's function at zero frequency  $G_{\mathbf{k}}^{-1}(0) = \mu - \epsilon_{\mathbf{k}} - \Sigma_{\mathbf{k}}(0)$  is needed to determine the topology of the quasiparticle states, since renormalization does not change the non-trivial topological nature of the bulk system. Following Refs. [31], we compute the topological invariant of an interacting system with the Hamiltonian defined by  $H_t(\mathbf{k}, \omega) = H(\mathbf{k}, \omega) + \Sigma_{\mathbf{k}}(0) - \mu$ . A modified effective dispersion of  $H_t(\mathbf{k})$  for which we neglected the imaginary part of  $\Sigma_{\mathbf{k}}(0)$  is given in the lower panel of Fig. 7. By introducing correlations, the bandwidth is reduced by approximately half, but the band inversion character still exists. According to the parity criteria, we conclude that  $\text{FeSe}_{0.5}\text{Te}_{0.5}$  remains a topological correlated system. The topological surface state is derived from this modified effective TB Hamiltonian.